Novel insights into the distribution and effects of perfluorooctanesulfonic acid (PFOS) in the nervous system of a frog tadpole model by mass spectrometry imaging

Rikke Poulsen, Emma M. Field, Angela M. Jackson, Haley Kuecks-Winger, Anita A. Thambirajah, David R. Goodlett, Caren C. Helbing, and Helena Pětrošová

2026

Environmental Science & Technology

pubs.acs.org/est

Article

Novel Insights into the Distribution and Effects of Perfluorooctanesulfonic acid (PFOS) in the Nervous System of a Frog Tadpole Model by Mass Spectrometry Imaging

Rikke Poulsen,* Emma M. Field, Angela M. Jackson, Haley Kuecks-Winger, Anita A. Thambirajah, David R. Goodlett, Caren C. Helbing, and Helena Pětrošová*

Cite This: *Environ. Sci. Technol.* 2026, 60, 3121−3134

Read Online

ACCESS | Metrics & More | Article Recommendations | Supporting Information

ABSTRACT: Determining how environmental contaminants localize within tissues is essential for understanding the consequences of sublethal exposures. Therefore, we optimized a mass spectrometry imaging (MSI) workflow to study the distribution and biological effects of contaminants in an environmentally relevant frog tadpole model. We applied the method to the entire tadpole head postexperimental exposure to the legacy contaminant, perfluorooctanesulfonic acid (PFOS; 0.1−100 μg/L, 48 h). At 10 μg/L, PFOS unexpectedly localized mainly to the olfactory epithelium. At 100 μg/L, PFOS was distributed throughout all tissues except for the brain, where only the pineal gland showed significant accumulation. The pineal gland, a neuroendocrine organ regulating the circadian rhythm, is not protected by the blood−brain barrier. Together, these findings indicate that PFOS did not readily cross the blood−brain barrier. In both the olfactory epithelium and pineal gland, effects of PFOS were reflected in changes in the abundances of endogenous lipids. The results open questions for the most adverse outcomes of PFOS exposure, including effects on the olfactory-mediated behavior and circadian rhythm. The present study exemplifies how MSI advances our analytical toolbox. The ability to localize contaminants within biological compartments is critical for the characterization of their toxic effects and risks to wildlife and humans.

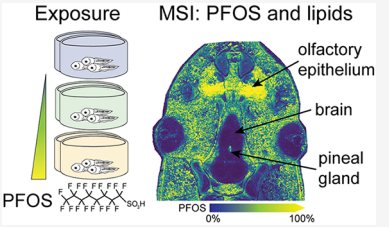

KEYWORDS: *mass spectrometry imaging, MALDI-MSI, PFOS, PFAS, amphibians, tissue distribution, lipidomics, olfactory system*

1. INTRODUCTION

Mass spectrometry imaging (MSI) is an exciting technology that adds spatial information to mass spectrometry analysis, allowing the mapping of specific molecules in the tissue. This is particularly interesting in the brain and olfactory sensory system, where different regions of the brain have distinct functions. Herein, we utilized a matrix-assisted laser desorption/ionization (MALDI) MSI method and the cosmopolitan American bullfrog (*Rana [Lithobates/Aquarana] catesbeiana*) and created a highly relevant biological model to study the tissue distribution of environmental contaminants.

The conventional mass spectrometry-based analytical methods to investigate bioaccumulation of contaminants involve tissue homogenization to extract and quantify the compound in question. These techniques are powerful. However, the tissue heterogeneity is lost in the process.[1] Additionally, extremely small tissues or tissue regions can be difficult to extract without contamination from the surrounding tissues; for example, the functional regions of the brain and its associated glands. In contrast, MSI circumvents these limitations, profiling the spatial distribution of molecules in the tissue, including pollutants.[2−7]

Per- and polyfluoroalkyl substances (PFAS) make up a large, diverse group of synthetic chemicals that are widely used in consumer products. Their persistence, bioaccumulation, and biomagnification in animal tissues are of great concern and have been linked to numerous deleterious health effects in animals and humans.[8−11] These effects include disruption of the endocrine system (especially the thyroid axis),[12] altered immune system function,[9] behavioral and cognitive disorders,[10] and adverse reproductive and developmental outcomes.[9] The last category includes a link to neurodevelopmental toxicity, such as disrupted neurotransmitter levels, myelination, and interneuronal signaling, which has been connected to autism spectrum disorders.[13]

One legacy PFAS, perfluorooctanesulfonic acid (PFOS), was extensively used in numerous consumer products. For example, it was added as a stain repellent for carpets, fabrics, upholstery, and food packaging, a surfactant in firefighting foams, and a key ingredient in fire-resistant aviation hydraulic fluids and photolithographic chemical mixtures. Although the use of PFOS is now prohibited or restricted in many places, its production persists in some global industries. In addition, the

Received: December 4, 2025
Revised: December 17, 2025
Accepted: December 18, 2025
Published: January 21, 2026

https://doi.org/10.1021/acs.est.5c17483
Environ. Sci. Technol. 2026, 60, 3121−3134

degradation of PFOS precursors can also act as its source.[14−16] The compound is highly resistant to degradation and biotransformation, it bioaccumulates in animal tissues, and can be transferred to offspring.[17−22] As a result, PFOS continues to be detected in the environment at very high concentrations, especially after its release from point sources, such as firefighter training grounds.[23,24] For instance, sampling of wastewater and runoff from a major firefighter training ground in France contained an average and a maximum PFOS concentration of 57 and 892 μg/L, respectively (n = 22 samples).[25] In the wastewater treatment plant outlet from the same training area, an average PFOS concentration of 25 μg/L was detected (n = 7 samples).[25]

Amphibians are exceptional models to study developmental toxicology, as they are extremely sensitive to changes in their surrounding environment.[26−28] Their eggs lack a protective shell or membrane, and their developing larvae are exclusively aquatic. Therefore, amphibians are directly exposed to surface water contaminants throughout their development. Tadpole metamorphosis, where a tadpole transitions into a frog, requires extensive reprogramming and reorganization of organs and tissues.[27,29−31] This process has direct parallels to the developmental transition of other vertebrates, including humans.[32] Hence, interspecies extrapolations are possible during this highly sensitive developmental window. Taken together, amphibians are excellent sentinels for the study of the tissue distribution of the environmental contaminants and their impact on the organism's development. Herein, we utilized a representative of true frogs, the cosmopolitan tadpole model American bullfrog (*Rana [Lithobates/Aquarana] catesbeiana*), to create an environmentally relevant model that can be used as a bioindicator.

MALDI-MSI has been previously used to determine the distribution of PFOS in murine liver, kidney, and cardiac tissue upon experimental exposure by oral gavage or gastric infusion.[3−6] Liquid extraction surface analysis mass spectrometry (LESA-MS) at a resolution of 600 μm has furthermore been applied to whole adult zebrafish.[33] Another related compound of known health concern, perfluorooctanoic acid (PFOA), has also been successfully detected by MALDI-MSI in mouse skin after dermal application to show tissue penetration[34] and in zebrafish to show whole-organism tissue distribution.[35] To the best of our knowledge, MALDI-MSI has not been applied to investigate PFOS distribution and effects in an environmentally relevant animal model following an exposure that mimics a realistic scenario during a critical window of development. Therefore, we developed an MSI workflow suitable for the investigation of the spatial distribution of contaminants in tadpole tissues and the associated biological effects. It enabled us to analyze 10 μm sections of the entire tadpole head, including the olfactory system, eyes, and brain. We then validated the method via a PFOS exposure study. Five PFOS concentrations were used, ranging from the European limit for the maximum total PFAS in drinking water (0.1 μg/L)[36] to the worst-case scenario of PFOS release from a point source (100 μg/L).[24] The approach expands the analytical toolbox for the unbiased screening of contaminants and their distribution and effects in wildlife biological compartments. The novel biological insights reported herein will allow the formulation of new hypotheses on developmental neurotoxicity caused by PFOS exposure, advancing environmental and toxicology research.

2. MATERIALS AND METHODS

2.1. PFOS Exposure

2.1.1. Animal Housing and Care. Premetamorphic *Rana [Lithobates/Aquarana] catesbeiana* tadpoles of mixed sex were caught locally, around Victoria, British Columbia, Canada (approximate 48.472285, −123.473600). They were housed at the University of Victoria Outdoor Aquatics Unit in 100-gallon covered fiberglass tanks containing recirculated dechlorinated municipal water at 15 ± 1 °C, pH 6.8, and 96−98% dissolved oxygen. The tadpoles were fed daily with Spirulina (Aquatic ELO-systems, Inc., FL). The care and treatment of animals was in accordance with guidelines established by the Canadian Council on Animal Care, and Animal Ethics Protocol AE-23−005−01 was approved by the Animal Care Committee of the University of Victoria.

2.1.2. Animal Exposure. The exposure was conducted in 12 L polypropylene buckets that were aerated with an air stone and maintained at 24 °C by standing them in shallow, temperature-controlled water trays. Each bucket contained 8 L of treatment water and three premetamorphic tadpoles (average body weight reported in Table S2). There were 2 buckets per treatment, giving a total of six animals per treatment (see Figure S1 for experimental setup). The nominal exposure concentrations were: 0, 0.1, 1, 10, 50, and 100 μg/L PFOS. The animals were not fed during acclimation or exposure. The water tray temperature was measured daily, and water quality parameters (pH, ammonia, nitrate, and nitrite) were tested daily with test strips (HACH, London, ON, Canada) (Table S1).

Prior to exposure, the tadpoles were acclimated in dechlorinated water in their respective buckets for 24 h. All tadpoles were then injected with a low dose of thyroid hormone thyroxine (T4) to start their metamorphic trajectory. They were briefly immobilized on dechlorinated ice and weighed on a digital laboratory scale in preparation for the T4 injection. Then, 1 μL/g bw rounded to the nearest 0.5 μL of 5 μM T4 (Sigma-Aldrich, purity ≥ 98%) in 400 μM sodium hydroxide (NaOH) solvent[37] was injected intraperitoneally via the tail muscle[38] using a 50 μL Hamilton syringe with 26 G × 1/2" sterile needles. While the animals were out of the bucket, the treatment solution was added to the buckets in a 10 mL stock solution (0.08−80 mg/L PFOS) (CAS: 2795−39−3, purity >95%, Toronto Research Chemicals, Canada) in ultrapure water (LC/MS grade, Optima, Fisher Scientific) or plain ultrapure water for controls. To avoid operator bias, the experiment was performed blinded by color-coding the treatments. The blinding was maintained through the data collection for physiological end points (i.e., weight and morphological characteristics) and serum analysis by LC-TIMS-MS. However, for the MSI and brain homogenate analysis, it was necessary to know the treatments.

2.1.3. Sample Collection. At termination, the animals were anaesthetized and euthanized by immersion in 0.1% (w/v) tricaine methanesulfonate (TMS; Syndel Laboratories, BC, Canada) and 25 mM sodium bicarbonate solution, followed by exsanguination. Weight and morphological characteristics were recorded. Blood samples were then collected from an incision made in the tail proximal to the body, allowed to coagulate for at least 15 min at room temperature, and spun down at 10,000g for 10 min at 4 °C. The serum was transferred to a new microcentrifuge tube and stored at −80 °C until analysis.

https://doi.org/10.1021/acs.est.5c17483
Environ. Sci. Technol. 2026, 60, 3121−3134

The tadpole heads for MSI analyses were dissected with a focus on preserving the tissue integrity of the brain. Hence, the entire section from the mouth to the top of the head was embedded in M-1 Embedding Matrix (Epredia, Netherlands; <1% carboxymethylcellulose) using plastic molds. Samples were then snap frozen by floating in vapors of liquid nitrogen and stored at −80 °C until analysis.

To verify the PFOS exposure concentrations, water samples (1 mL) were collected from all buckets immediately after treatments were added, before the animals were released back to the buckets (t0) and again at project termination after 48 h (t48). The water samples were stored at −80 °C until analysis.

2.2. Mass Spectrometry Imaging of Tadpole Tissues

2.2.1. Sample Preparation. We selected three treatment groups for MSI analysis: controls (0 μg/L), 10 μg/L, and 100 μg/L of PFOS; n = 5 animals per group. Samples were cryosectioned horizontally to 10 μm thickness using a cryotome (CM1950, Leica Biosystems) set to −12/−10 °C (chamber/specimen head) and C-35 microtome blades (Feather Safety Razor Co., Osaka, Japan). Tape transfer (Tesa FILM double-sided, Tesa SE, Norderstedt, Germany) was used to maintain the structural integrity of these highly heterogeneous and friable samples. The taped sections were mounted on ITO slides (part no. CB-90IN-S111, Delta Technologies, Loveland, CO) and excess tape cut away with a scalpel. Each slide contained three samples, one from each of the treatments: control, 10, and 100 μg/L, and five slides were analyzed (n = 5 animals analyzed per treatment, N = 15 animals analyzed in total). Furthermore, one animal from the highest exposure group (100 μg/L) was used to investigate the extent of the PFOS signal detected in the brain. In this case, three sections from that same animal at different sectioning planes were mounted on the same slide. See Figure S2 for slide overview.

One microliter of Splash Lipidomix standard mix (1 μL, Avanti Research, Alabama) was spotted on all slides to monitor instrumental fluctuations. Additionally, a small area of tape-mounted tissue from below the brain region was cut into five separate rectangles, and 1 μL of PFOS standards (0.1, 1, 10, 100, and 1000 μg/L) was spotted onto them. It was important to spot the standards on the tissue to account for ion suppression and enhancement due to the tissue matrix.

The slides were then sprayed with norharmane matrix solution for nontarget analysis in negative ionization mode. Norharmane (98% TLC, Sigma-Aldrich) was dissolved in chloroform:methanol (2:1) at a concentration of 7 mg/mL and applied with an automated sprayer (HTX M5 Sprayer, HTX-Technologies LLC) using the following settings: solvent flow rate of 120 μL/min; nitrogen pressure of 10 psi; nozzle spray temperature of 30 °C; plate temperature of 25 °C; 12 passes (criss-cross pattern) with 30 s drying time; nozzle spray head height set to 40 mm; nozzle head velocity of 1200 mm/min; and track spacing of 3.0 mm.

Prior to the slide being placed in the instrument, the adhesiveness was evaluated by applying compressed air to the tape. This is why some of the small rectangles containing PFOS standards are absent on certain slides (see Figure S8D for example).

Investigation of signal suppression and enhancement by different tissue types in the sample was performed by spraying a nonexposed tadpole section with norharmane matrix containing 0.5 mg/L PFOS (Figure S4). Linearity and sensitivity of the method were assessed using a 10-point standard curve (2−1000 μg/L) spotted on a nonexposed tadpole section (Figure S5). Using the quantitation module in SCiLS Lab software (Version 2025a Pro, Bruker Daltonics), the limit of detection (LOD) was estimated by the standard deviation (SD) of the blank and of the lowest standard (2 μg/L). First, the limit of the blank, LoB, was calculated as LoB = $\text{mean}_{\text{blank}} + 1.645 \times \text{SD}_{\text{blank}}$, and then LoD = LoB + $1.645 \times \text{SD}_{\text{low}}$.

2.2.2. Data Acquisition. Matrix-assisted laser desorption/ionization (MALDI)-MSI analysis was performed on a timsTOF fleX MALDI-2 instrument (Bruker Daltonics GmbH, Germany). The mass range was set to m/z 500−1500, and trapped ion mobility (TIMS) was used. The broad mass range was selected to make a versatile method, with applicability to a range of contaminants, and to be able to also study effects on biomolecules. To ensure method transferability to other instruments, only the primary laser was used (i.e., no secondary ionization). A pixel size of 50 μm × 50 μm was used in all experiments, except those reported in Figure 3. In this subset of samples, the olfactory epithelium and pineal gland regions were imaged at 20 μm spatial resolution. The laser frequency was set to 10 kHz with 999 shots accumulated at each pixel. Custom laser focus was manually adjusted to account for the extra height added to the tape. Table S4 lists the method parameters.

Before each imaging experiment, calibration was performed in electrospray (ESI) mode using a direct infusion of the Agilent electrospray ionization (ESI) liquid chromatography−mass spectrometry (LC-MS) tuning mix (Agilent Technologies, Santa Clara, CA). Ions in the scan range were used for calibration (m/z = 666.01879, 1033.9881, and 1333.9689). In addition, an online calibration was utilized to correct for any mass shifts that could occur during the imaging run. The following ions were used for the online calibration: m/z 885.5499 (monoisotopic mass of $[\text{PI(38:4)-H}]^-$), m/z 515.1620 (monoisotopic mass of $[\text{NOR-H}]^-$), m/z 1447.9650 (monoisotopic mass of $[\text{CL(72:8)-H}]^-$), and m/z 1449.9806 (monoisotopic mass of $[\text{CL(72:7)-H}]^-$). The resulting mass accuracy was evaluated using the $[\text{PI(38:4)-H}]^-$ ion (m/z 885.5499) and was 2.5 ppm across the data set. On all slides, small areas of matrix only (no tissue, embedding medium, or tape) and matrix on embedding medium and tape (no tissue) were analyzed as negative controls (Figure S2). Splash Lipidomix standard mix (Avanti Research, Alabama) was spotted on all slides to monitor fluctuations between runs. Some minor fluctuations were observed, but there were no clear trends of increasing or decreasing sensitivity over the scanned range (Figure S3). Finally, PFOS standards (0.1−1000 μg/L) were spotted on small squares of tissue on each slide as positive controls.

2.2.3. Postacquisition Hematoxylin/Eosin Staining. After MSI data acquisition, the samples were hematoxylin/eosin (H&E) stained to visualize the morphological features of the tissue. Modifications were necessary to facilitate staining on the samples mounted with the adhesive tape. Initially, the matrix was removed in 3 changes of ice-cold methanol (Optima LC/MS grade, Fisher Chemical), and samples were fixed for 1 h in 10% formalin (Sigma-Aldrich, Oakville, CA). The tissue was then rehydrated with changes in ethanol series (2 min each): 100%, 100%, 90%, 70%, 50%, followed by 2 min in water. The slides were stained in Gills No. 2 hematoxylin for 30 s (Sigma-Aldrich, St. Louis) and rinsed quickly in 2 changes

https://doi.org/10.1021/acs.est.5c17483
Environ. Sci. Technol. 2026, 60, 3121−3134

of water, followed by 3 dips in 1× Scott's modified tap water solution (0.02% sodium bicarbonate, 0.2% anhydrous magnesium sulfate), followed by 30 s in acidified eosin Y (0.25% in 80% Ethanol, Fisher Chemical, India). The slide was washed and dehydrated with an ethanol series (2 min each). Further dehydration in xylene is not compatible with the tape. Finally, coverslips were mounted directly on the tape, and the slides were scanned at 10,000 dpi with a PathScan Enabler 5 scanner (Meyer Instruments, Houston).

2.2.4. Data Analysis. Data were processed and analyzed in SCiLS Lab (Version 2025a Pro, Bruker Daltonics). The PFOS ion images were created upon root-mean-square (RMS) normalization. To uncover the effects of PFOS on endogenous lipids in tissue, three regions of interest (myelin layers of the brain, olfactory epithelium (OE), and the pineal gland) were outlined based on the postacquisition H&E staining using the brush tool in SCiLS. Next, the non-normalized data from these regions were exported in the imzml format and imported into R (version 4.4.3),[39] where the package Cardinal (ver 3.8.3)[40] was applied using R Studio (version 2023.12.1.402).[41] Mass spectra from the individual regions were grouped according to the tissue type. Data were then normalized by RMS, and the peaks were processed using the default settings for peak picking (threshold of signal-to-noise of 3, mass tolerance of 10 ppm, and filtering away the 10% lowest intensity peaks). Treatment groups (control, 10 μg/L, and 100 μg/l) were defined based on sample location on the slide, and a linear mixed model was fitted to identify statistically significant differences (FDR < 0.1) between treatments. The high false discovery rate was accepted for this initial screen of interesting compounds. For the OE, this approach gave more than 300 molecular features that differed significantly between the controls and groups exposed to PFOS, so FDR < 0.05 was used instead.

A list of molecular features of interest displaying significant changes in abundance in response to PFOS exposure was manually curated by checking the peak shape, intensity, and integration. All molecular features that did not meet the quality control criteria were excluded. Additionally, molecular features that were identified as part of the exposome were taken out of the effects analysis (see Section 3.5, Figure S15−S16, and Table S10 for these PFOS impurities). The compounds remaining after filtration were analyzed by a linear mixed model of the R-package "lme4"[42] adjusted for possible batch effect (e.g., slide). Model checking was performed by visual assessment of QQ-plots and residual plots followed by a posthoc pairwise comparison by t tests (Tukey contrasts).[43] For each analysis, a prespecified significance level of $p \leq 0.05$ was used. Abundance of significantly affected molecular features was visualized as heatmaps with Euclidean clustering on rows and no clustering on columns using the Pheatmap R-package.[44]

2.2.5. Annotation of Molecular Features. Molecular features remaining after data filtration were annotated according to the identification level system specified in Viant et al.[45] Initially, the MSI data was analyzed in Metaboscape with a search for Lipid Species (Version 2022b Pro, Bruker Daltonics) using the m/z, collision cross section (CCS, as measured using TIMS), and mSigma (deviation of a measured isotopic pattern from the predicted one) values. The resulting lists were matched to the annotated lipidomics data sets obtained from tadpole brain homogenates by liquid chromatography tandem mass spectrometry (LC-MS/MS; see Section 2.3 below) and in-house tandem mass spectrometry libraries. If the annotations were inconsistent, then the annotation was based on mass spectrometry results directly from tissue.

2.3. High-Resolution Mass Spectrometry Analysis of Brain Homogenate and Serum

2.3.1. Sample Preparation. *2.3.1.1. Brain Homogenate.* After the sections for MSI were obtained, the rest of the brain was extracted from the cryopreserved tissue blocks and transferred to 2 mL Safe-Lock tubes (Eppendorf, Mississauga, CA) for bead beating (n = 6 per concentration, N = 36 in total). The samples from groups not used for MSI (exposure concentrations 0.1, 1, and 50 μg/L) were sectioned to the same depth to ensure nonbiased comparison between the samples. The extraction followed the procedure published in Post et al.[46] All solvents used were of LC/MS grade (Optima, Fischer Scientific). In brief, the samples were homogenized by bead beating with two metal beads (2 s × 30 s, 25 Hz) in 800 μL of ice-cold methyl-t-butyl-ether:methanol (10:3) containing butylated hydroxyltoluene (12.5 μg/mL) as an antioxidant and 5 μL of internal lipid standard mix (Splash Lipidomix). Subsequently, 200 μL ice-cold 0.1% formic acid was added to induce phase separation. After further bead beating (3 s × 30 s, 25 Hz), the samples were left on ice for 10 min before centrifugation (15,000g, 15 min). The supernatant was transferred to a high-performance liquid chromatography (HPLC) vial (Agilent, Mississauga, CA), evaporated under nitrogen (37 °C), and reconstituted in mobile phase A (see below in Section 2.3.2).

2.3.1.2. Serum. Serum samples (n = 6 per concentration, N = 36 in total) were extracted, as specified for plasma in Post et al.[46] In brief, 20 μL of serum was combined with 1 mL of ice-cold MTBE:MeOH (10:3), and 5 μL of Splash Lipidomix standard mix was added. After vortexing for 1 min (4 °C, 1400 rpm), 250 μL of water was added, and the samples were vortexed for 45 min (4 °C, 1400 rpm). After leaving the samples to equilibrate on ice for 10 min, the samples were centrifuged (4 °C, 15,000g, 10 min), and the supernatant was moved to an HPLC vial, evaporated under nitrogen (37 °C), and reconstituted in mobile phase A (see below in Section 2.3.2).

2.3.2. Data Acquisition and Analysis. The samples were analyzed on a UHPLC-TIMS-MS platform, which consisted of a Bruker timsTOF flex MALDI-2 (Bruker Daltonics GmbH, Germany) hyphenated with a Thermo Fisher Vanquish ultrahigh performance liquid chromatography (UHPLC) system (binary pump, degasser, and autosampler; Thermo Fisher Scientific). The analytical column (Avantor ACE Excel 2, 2.1 mm × 100 mm, 2 μm, C8-phase) was maintained at 55 °C. The injection volume was set to 10 μL. Mobile phase A was water:isopropanol:acetonitrile 2:1:1 with 0.05% acetic acid, 20 μM phosphoric acid, and 5 mM ammonium acetate. Mobile phase B was isopropanol:acetonitrile 1:1 with 0.05% acetic acid and 5 mM ammonium acetate. The flow rate was 0.6−1 mL/min, and the gradient was as specified in Table S3. The timsTOF flex was operated in negative ionization mode with settings as in Table S4. Like the MSI method, the mass range was set to m/z 500−1500. Also, here, a broad mass range was selected to make a versatile method with applicability to a range of contaminants and to be able to also study effects on biomolecular levels. An online recalibration was performed at the beginning of each sample acquisition using the Agilent ESI

https://doi.org/10.1021/acs.est.5c17483
Environ. Sci. Technol. 2026, 60, 3121−3134

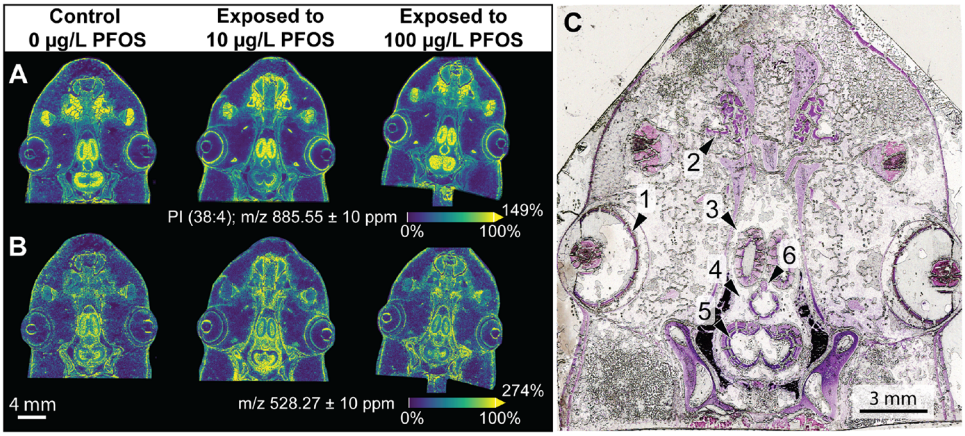

Figure 1. Image quality obtained with the developed MSI methodology. (A) distribution of a phosphoinositol (m/z 885.55, $[PI(38:4)\text{-}H]^-$) and (B) distribution of an unidentified molecular feature (m/z 528.27). Root-mean-square normalization was applied. The colored bar gives a visual map of the ion intensities; 100% on the scale represents a 95% quantile threshold, and the maximum measured intensity is displayed as a percent value relative to the 95% cutoff (i.e., all pixels with measured intensity above ≥95% appear bright yellow). (C) Postacquisition hematoxylin and eosin (H&E) stain of the tissue. Arrows point toward the following distinguishable tissue structures: 1: retinal layers of the eye, 2: olfactory epithelium, 3: telencephalon, 4: diencephalon, 5: tectum, and 6: pineal gland.

LC-MS tuning mix injected directly into the ESI source via a syringe pump. For this, the 15 min LC-MS runtime was divided into two segments, with the first segment (0.0 to 0.3 min) used for the injection of tune mix, and the last segment (0.3−15 min) used for the sample data acquisition. The switch between the segments was achieved using a conventional 6-port divert valve.

Data was processed and analyzed in MetaboScape (Version 2022b Pro, Bruker Daltonics). Annotation was based on a search for Lipid Species using the m/z, CCS, and mSigma (deviation of a measured isotopic pattern from the predicted one) values. The resulting lists were matched to a lipidomics data set obtained from another tadpole data set (UHPLC-TIMS-PASEF-MS data acquisition on serum and brain), which was annotated using the spectral libraries from MSDIAL and Bruker NIST incorporated in MetaboScape. A cutoff criterion of MS^2 score >600 was used. Lipids were classified based on the LIPID MAPS system.[47]

For dose−response modeling, the log-transformed peak areas were exported from MetaboScape and imported into R. After missing value imputation by the half minimum method, the R-package DRomics[48,49] was applied to uncover features with a dose−response relationship. Features that significantly changed in abundance in responses to increasing PFOS exposure were preselected using a quadratic trend test with an FDR < 0.1, and subsequently, dose−response models were fitted to these features. The method used to select the best fit is based on an information criterion as described in Larras et al.[49] The benchmark dose (BMD) was calculated as the so-called BMD-zSD, which considers the residual standard deviation of the fitted concentration−response curve.[49]

2.4. Exposure Verification by LC-MS/MS

Ten microliters of isotopically labeled $^{13}C_8$−PFOS (cPFOS, 650 µg/L) (purity >99%, Cambridge Isotope Laboratories, Tewksbury, MA) was added to 250 µL water samples collected before and after the animals were added to the buckets. After a quick vortex to mix, the sample was transferred to a filtration tube (Nanosep with 0.2 µm Bio-Inert, Life Sciences) and centrifuged (10 min, 14,000 rpm). Two hundred and 50 microliters of the sample were then transferred to HPLC vials. The quantification was performed on an Agilent 6495c triple-quadrupole system with a hyphenated Agilent 1290 Infinity II ultrahigh performance liquid chromatography (UHPLC) system (binary pump, degasser, and autosampler; Agilent Technologies). Targeted analytes were PFOS and cPFOS (Limit of detection 0.01 ng/mL; Limit of quantification 0.03 ng/mL). A neat standard ten-point calibration curve (0.01 − 100.0 µg/L) was prepared in Milli-Q water. All vials contained a fixed amount of internal standard (25 µg/L). See Supporting Information S2 and Table S5 for further details on the analytical method. Data was analyzed in Agilent MassHunter − Quantitative Analysis (QQQ) version 10.1.

3. RESULTS

3.1. Optimization of the MSI Methodology

We first developed an MSI methodology that enabled us to analyze 10 µm sections of the entire tadpole head, including the olfactory system, eyes, and brain. The optimized sample preparation method made it possible to obtain these cryosections with an intact morphology, despite the high heterogeneity of the sample. An application of tape for transferring the tissue section to the slide was the primary factor contributing to this improvement (Figure S6). Phospholipids are structural components of cells and were also captured using our data acquisition method. Spatial distribution of some of these molecules, such as phosphatidylinositol, PI (38:4) with m/z of 885.55, correlated with morphological features of the tissue sample. Therefore, we used this molecule to showcase the general tissue structure and integrity (Figure 1A). Another, yet unidentified, molecular feature (m/z 528.27) also consistently provided a clear structural definition of this complex region (Figure 1B). The postacquisition H&E staining allowed further unambiguous identification of tissue structures, including individual brain regions (e.g., telencephalon, diencephalon, tegmentum, and gray and white matter), the olfactory epithelium, and the retinal layers of the eyes (Figures 1C and S10D−F). In conclusion, the sample preparation method is appropriate for investigating the distribution of contaminants in the tissue along with their potential localized effects on biomolecules.

https://doi.org/10.1021/acs.est.5c17483
Environ. Sci. Technol. 2026, 60, 3121−3134

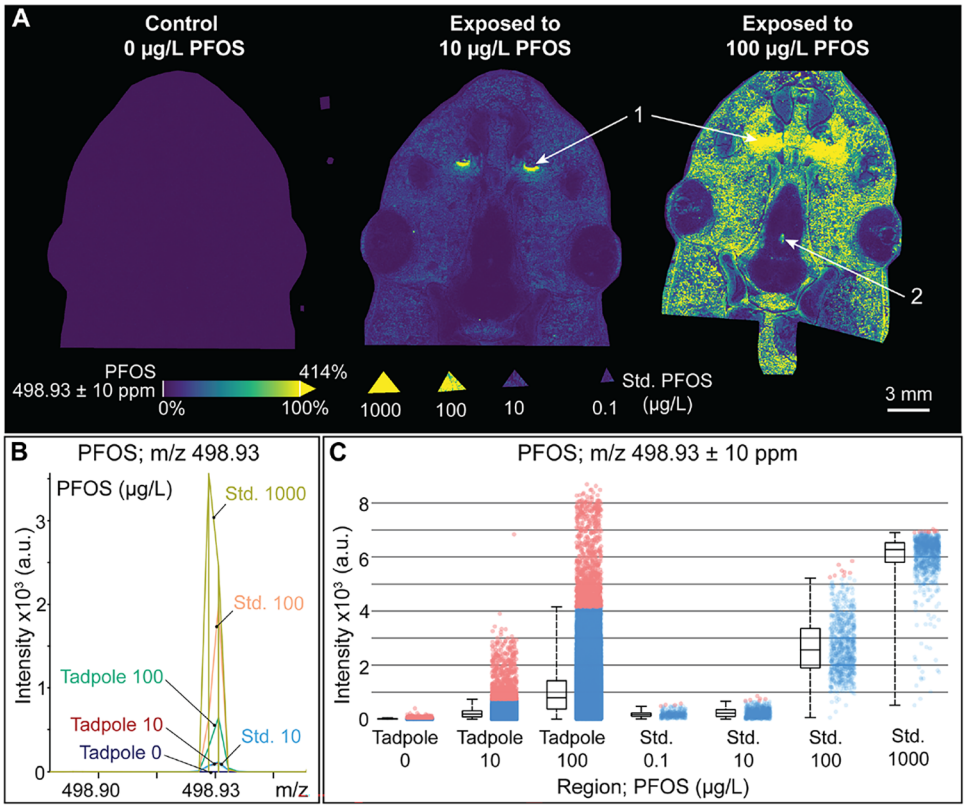

Figure 2. Distribution of PFOS. (A) PFOS (m/z 498.93 ± 10 ppm) recorded by MSI in three treatment groups (from the left: negative control, 10 μg/L PFOS, and 100 μg/L PFOS exposure). The data were recorded in negative ionization mode on a Bruker timsTOF fleX MALDI-2 at a spatial resolution of 50 μm. Root-mean-square normalization was applied. The colors indicate scaled ion intensity from blue (low) to yellow (high). The color bar gives a visual map of these intensities, and the maximum intensity is displayed as a percent value relative to the 95% quantile intensity cutoff. Arrow 1 points toward the olfactory epithelium. Arrow 2 points out the pineal gland. The triangles show PFOS standards spotted on the tissue (0.1−1000 μg/L). (B) Absolute intensity of the recorded PFOS signal (m/z 498.93 ± 10 ppm) in tadpole sections and in the spotted standards. (C) Intensity box plots showing the signal intensity of PFOS in tadpole sections and in the spotted standards. The box shows the median intensity of the recorded region, the lower and upper bounds of the box represent the second and third quantiles, and whiskers represent the lower (0%) and upper (95%) quantiles. The dots show the distribution of the measured PFOS intensities; blue and red dots represent pixels with intensity below and above the 95% quantile, respectively.

3.2. Distribution of PFOS in the Tadpole Nervous System

Our second objective was to validate the developed method within the context of a PFOS exposure study. We tested five concentrations, ranging from 0 μg/L (control group) to a worst-case scenario of PFOS release from a point source (100 μg/L). Altogether, six treatment groups with six animals per group were included. Of those, three treatment groups were selected for MSI analysis: 0 μg/L (controls), 10 μg/L, and 100 μg/L of PFOS, with five animals analyzed per treatment group. The resulting tissue sections were distributed across five microscopic slides, so that each slide contained one tissue section per treatment group (0 μg/L, 10 μg/L, and 100 μg/L). A representative image of one of the five slides is shown in Figure 2A. The remaining images can be found in the Supporting Information (Figures S7−S10).

First, a nonexposed tadpole section was sprayed with norharmane matrix containing 0.5 mg/L PFOS to investigate signal suppression and enhancement by different tissue types in the sample. The signal showed a minor signal suppression in the myelin-rich area of the brain and minimal variation across the sample, except from two smaller spots, and this could be attributed to microbubbles and texture differences in the tape (Figure S4). The linearity and sensitivity of the method were then assessed using a 10-point standard curve (2−1000 μg/L) spotted on a nonexposed tadpole section (Figure S5). The initial linear range was estimated to be 0−30 μg/L PFOS; a higher concentration led to signal saturation (Figure S5C,D). At 2 μg/L PFOS, the signal intensity was still distinguishable from the noise. The LOD was estimated to be 1.5 μg/L. The tape did not introduce any interfering impurities (Figure S11).

Using our refined MSI method, we then obtained unprecedented and unbiased information about the distribution of PFOS in tadpole tissue upon experimental exposure (Figures 2A and S7A−S10A). Surprisingly, the legacy contaminant was localized mainly to the olfactory epithelium of tadpoles exposed to both 10 and 100 μg/L PFOS (Figure 2A, arrow 1). In tadpoles exposed to 100 μg/L PFOS, the compound was further distributed throughout all tissues (Figure 2A, arrow 1 and Figures S7−S10). Interestingly, little to no PFOS signal was detected in the brain of these animals, with the exception of the pineal gland, which showed substantial accumulation of PFOS (Figure 2A, arrow 2 and Figures S7A−S10A, arrow 2). The pineal gland is a neuroendocrine organ responsible for the synthesis of melatonin and regulation of the circadian rhythm. Unlike the rest of the brain, the gland is not protected by the blood−brain barrier.[50] Collectively, our findings suggest that either PFOS did not cross the blood−brain barrier or its concentration in

https://doi.org/10.1021/acs.est.5c17483
Environ. Sci. Technol. 2026, 60, 3121−3134

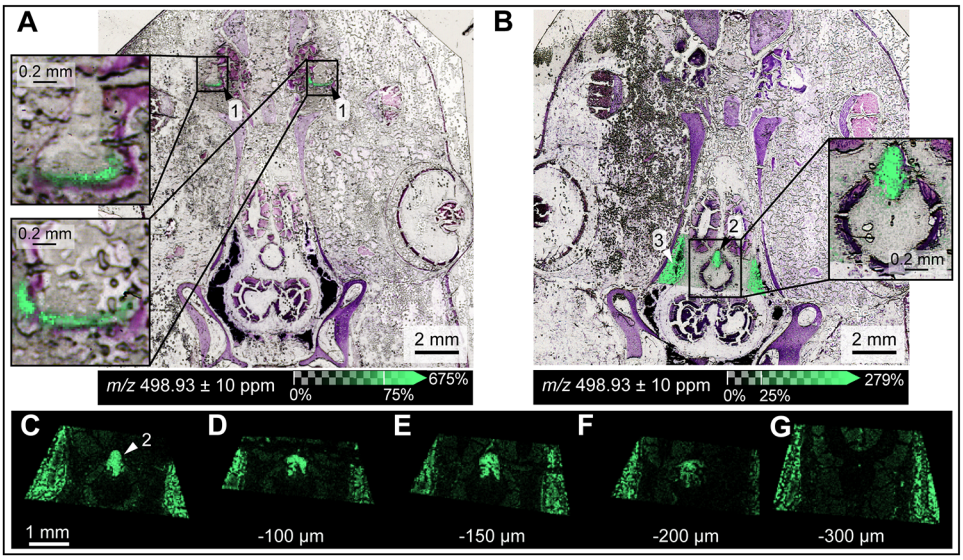

Figure 3. High-resolution (20 μm) images of PFOS hotspots overlaid on H&E stain. (A) Olfactory epithelium (OE) imaged in a tadpole exposed to 10 μg/L PFOS. Arrow 1 points to the OE. (B) Brain region containing the pineal gland imaged in a tadpole exposed to 100 μg/L PFOS. Arrow 2 points to the pineal gland, and arrow 3 points to the edge of the brain. To clarify how deep into the brain the PFOS signal went and to ascertain the association with the pineal gland, sections were sampled further down through the tissue at the following depths below the image shown in panels (C, D) −100 μm, (E) −150 μm, (F) −200 μm, and (G) −300 μm.

the majority of brain tissue was below the limit of detection of the method.

The quality of the PFOS signal in tissue was confirmed by examining the peak shape and its alignment with those of spotted PFOS standards (Figures 2B and S7B−S10B). Visualization of the median signal intensity of PFOS in the recorded regions by box plots (Figure 2C) showed the expected increase with concentration in both spotted standards and exposed tadpoles. Dot plots illustrating the distribution of individual spectral intensities (each dot representing one spectrum from one 50 μm pixel) also revealed the heterogeneity of the signal in the exposed tadpoles. Bearing in mind that the MSI is inherently not quantitative (Figure S5), the distribution of the spectral intensities recorded in the tadpoles exposed to 100 μg/L surpassed those recorded from the 1,000 μg/L standard, indicating a bioconcentration factor above 10 for certain tissue structures (Figure 2C). Overlaying the H&E stain with the MSI data to define tissue structures such as the pineal gland, olfactory epithelium, myelin layers of the brain, and retinal layer of the eye further facilitated a comparison of the PFOS signal intensities in different tissue structures within and between each exposure concentration (Figure S11).

Based on the results of the five replicates, we identified two areas of particular interest that warranted further investigation at higher spatial resolution: the olfactory region and the brain region around the pineal gland. Hence, a serial section was analyzed at a 20 μm resolution (Figure 3). First, PFOS localization to the olfactory epithelium was confirmed by overlaying these data with the H&E stain (Figure 3A). The localization to the pineal gland was also further confirmed by data acquisition at a 20 μm resolution (Figure 3B). To clarify how deep into the brain the PFOS signal went, additional sections were sampled deeper into the tissue. At 300 μm below the original sampling level, the distinguishable tissue structure disappeared together with a high PFOS signal (Figure 3C−G). Overall, this analysis confirmed that the PFOS signal in the center of the brain was localized specifically to the pineal gland.

3.3. PFOS in Brain Homogenate and in Serum

To validate the MSI model, we analyzed brain homogenate and serum by UHPLC-TIMS-PASEF-MS. We detected PFOS using this platform. As the exposure dose increased, the measured PFOS signal increased in brain homogenates (Figure 4) and serum samples (Figure S12). It is important to note that the pineal gland and meninges of the brain were sampled and included in the homogenates. Based on our MSI data showing a high concentration of PFOS in the pineal gland and

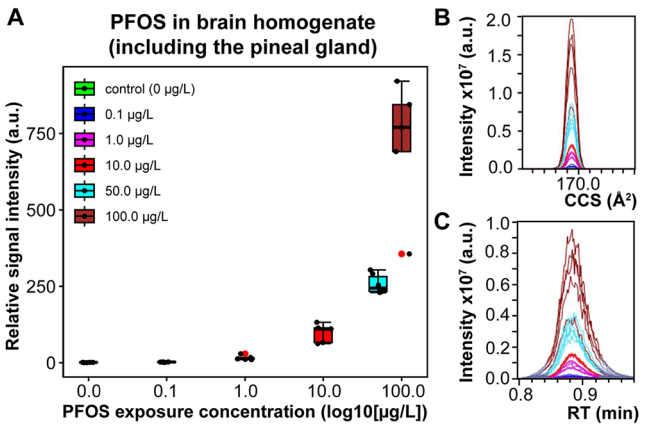

Figure 4. PFOS in brain homogenate, including the pineal gland. (A) Box plot of the relative PFOS signal intensity (compared to the control average and normalized to sample weight) as a function of the nominal exposure concentrations. The lower and upper hinges correspond to the first and third quartiles. The whiskers extend from the hinge to the largest/smallest value no further than 1.5 times the interquartile range. Circles show individual biological replicates (n = 6 per concentration). Outliers are indicated in red. (B) Ion mobility peaks and (C) chromatographic peaks exhibiting the non-normalized signal intensity.

https://doi.org/10.1021/acs.est.5c17483
Environ. Sci. Technol. 2026, 60, 3121−3134

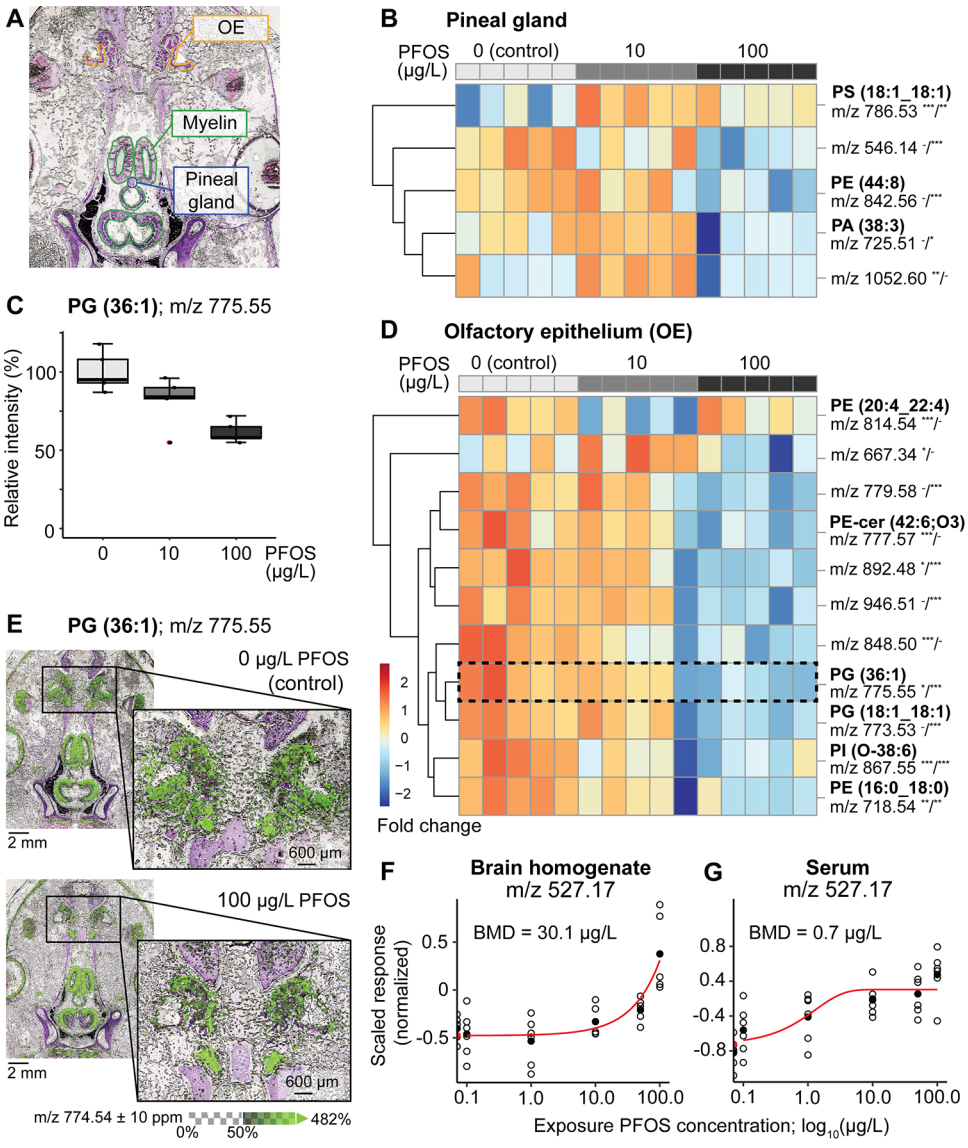

Figure 5. Effects of PFOS on the tadpole lipidome in target regions. (A) Visualization of the regions (olfactory epithelium (OE), myelin layers of the brain, and the pineal gland) that were defined based on H&E staining and used in statistical comparisons. (B) and (D) Heatmaps showing the endogenous molecular features displaying a significant difference in abundance in response to PFOS exposure in the pineal gland (B) and OE (D). Each column represents a replicate and each row a compound, for which the annotation is given (for details, see Table S7). Asterisks indicate a significant difference between the controls and tadpoles exposed to 10 μg/L (before the slash) and 100 μg/L (after the slash) of PFOS. (C) Example boxplot showing the levels of the lipid PG 36:1 in the OE-region in the control, 10, and 100 μg/L. (E) PG 36:1 (m/z 775.55 ± 10 ppm) signal recorded by MSI in a control tadpole and a tadpole exposed to 100 μg/L of PFOS. (F, G) Dose−response curve of the relative signal of an unidentified biomolecule of m/z 527.17 in the brain homogenate (F) and serum (G) across all tested concentrations of PFOS exposure. The estimated benchmark dose (BMD) based on the fitted model is listed. ***p < 0.001, **p < 0.01, *p < 0.05, and − p > 0.05.

next to none in the rest of the brain (Figures 2A and S7−S10), the measured PFOS signal in the homogenate was likely stemming from the gland.

3.4. Biological Effects of the PFOS Exposure

In addition to the distribution of contaminants, our MSI method allowed us to investigate localized effects on biomolecules. Linear mixed models were applied to the MSI data to statistically compare the effects of PFOS within the three regions: myelin tissue in the brain, the pineal gland, and OE revealed effects on several lipids in the pineal gland (Figure 5B) and OE (Figure 5D). Effects could be visually confirmed in the MSI data (Figure 5E). No myelin-specific effects were observed.

The nontarget UHPLC-TIMS-MS data for brain homogenate and serum further allowed investigation of dose−response relationships across all exposure concentrations. The analysis identified 21 biomolecular features in serum and 17 in brain homogenate that were significantly modulated by PFOS exposure in a dose-dependent manner, allowing for the application of dose−response modeling to the data. Figures S13 and S14 show the fitted dose−response models, and Tables S8 and S9 display the model parameters and benchmark doses (BMD) for these biomolecular features. The BMD is the dose corresponding to a predefined benchmark response (BMR), which indicates a significant change from the baseline. Some features were found to be affected in a dose-dependent manner in both serum and brain

https://doi.org/10.1021/acs.est.5c17483
Environ. Sci. Technol. 2026, 60, 3121−3134

homogenate, as exemplified by a compound with m/z 527.17 (Figure 5F,G). Even though this particular compound could not be annotated, its consistent response to PFOS exposure in two biological matrices underlines its potential utility as a biomarker.

3.5. Molecular Features Corresponding to PFOS Impurities

Trapped ion mobility (TIMS) was used to distinguish features belonging to the tadpole metabolome from those of the exposome. The technology separates molecules in a gas phase based on their mobility through an electric field, which is largely determined by their shape and size. Here, it allowed us to distinguish between endogenous biomolecules and halogenated xenobiotics (Figure S15). In total, eight features were found to be significantly affected by the PFOS exposure when compared to controls grouped in the space of halogenated xenobiotics. These compounds also had a close to identical spatial distribution to that of PFOS, as determined by MSI (Figure S16), and their measured intensity in tissue increased with the increasing PFOS exposure. However, these xenobiotics were also present in the PFOS standard, and their measured abundance increased proportionally to the increasing concentration of the spotted PFOS standard in positive controls (Figure S16). Hence, we concluded that they were not PFOS biotransformation products, but impurities in the PFOS standard used for exposure (95% purity standard used). Two features were part of the PFOS isotopic envelope (M + 1 and M + 2). Likewise, 11 features showing a significant dose−response relationship with PFOS exposure in the serum and brain homogenate were found to belong to the exposome (Figure S15 and Table S10).

4. DISCUSSION

An MSI methodology was developed, which enabled us to map contaminant and biomolecule distribution in the entire tadpole head, including the olfactory system, eyes, and brain. Despite the high heterogeneity of the sample, intact morphology was maintained during our workflow (Figure 1). The localization of contaminants is key to determining the molecular interactions that ultimately lead to adverse toxic effects.[51] This type of spatial mapping is particularly valuable in the brain, where small adjacent tissue regions have very distinct functions.

In the optimization of the MSI sample preparation, the main factor for maintaining sample integrity was the application of double-sided tape for transferring the tissue section to the slide. The application of tape transfer for MSI is not new,[52] and has, for instance, been applied to the MSI of bone[53] and mouse embryos.[54] To the best of our knowledge, this is the first application to obtain detailed images of the tadpole nervous system. To facilitate replication of our method, we have described special considerations for the tape transfer technique in the Supporting Information (Figure S6).

To estimate the analytical performance of our method, serial dilutions of the PFOS standard were spotted on a tadpole tissue section (2−1000 μg/L; Figure S5). The estimated limit of detection (LOD) was 1.5 μg/L PFOS. The linear range was estimated to be 0−30 μg/L PFOS (R^2 = 0.95). The applicability of MSI to detect and quantify PFOS has been previously investigated by Reynolds et al.,[55] utilizing a similar MSI platform to that in the present study. The authors assessed the linearity and limit of detection by spotting PFOS standards on a stainless steel MALDI plate. In contrast, the present method was assessed with standards spotted directly on tadpole tissue, accounting for biological matrix effects (e.g., ion suppression). The on-tissue detection range of our method was similar to that reported by Reynolds and colleagues.[55] Our linear range was narrower but more reflective of the biological matrix. Yang et al.[56] used PFOS standards spotted on murine kidney sections, but the concentration range was about 1000 times higher than here. To truly extend MALDI MSI methods to quantitative ones, a tissue mimetic model is needed. Development of such a model would lead to a significant loss of life due to the small size of the individual tadpole tissues. To comply with the 3 Rs (replace, reduce, refine) for animal experimentation, we deemed the model beyond the scope of the present study.

Our method enabled simultaneous detection of PFOS and endogenous biomolecules to determine exposure responses and toxicity. Among all five replicates, the 10 μg/L-treatment consistently resulted in localization of PFOS to the olfactory epithelium and minimal distribution to the other tissues. Additionally, the abundance of several lipids was significantly affected by PFOS in the olfactory epithelium. This finding is particularly noteworthy, as it suggests that the primary hazard of short-term PFOS exposure at environmentally relevant levels is associated with the olfactory system. This includes olfactory-mediated behavior (based on sensing of environmental cues) and remodeling of the olfactory epithelium that is essential during the metamorphic transition. Response to food and predator olfactory cues from the environment is essential for the survival and fitness of both tadpoles and frogs.[57] The olfactory epithelium, where PFOS accumulates, is a major component of the olfactory system. It lines the principal cavity, projecting inward from the animal's nares. The outer surface is covered with receptors that bind olfactory molecules, propagate the signal to the brain, and trigger a behavioral response.[58] To accommodate the transition from an herbivorous, aquatic tadpole to a carnivorous terrestrial frog, extensive remodeling of the olfactory system is needed.[58] This means that the olfactory system is one of the tissues that must undergo the most extensive remodeling during metamorphosis,[59] and this remodeling is dependent on the tissue-specific action of thyroid hormones. In fact, olfactory epithelium has been found to be one of the most thyroid hormone responsive tadpole tissues investigated to date[58,59] and may be employed as a sensitive bioindicator for the evaluation of disruption of the thyroid hormone system. Whole animal studies are required to investigate the behavioral implications of PFOS accumulation in the olfactory epithelium. Given the critical role of this tissue in mediating responses to food and predators, an impairment of its function could lead to decreased animal fitness and survival.

Following the highest tested exposure concentration (100 μg/L), PFOS was distributed throughout all tissues, while the signal was below the detection limit in the brain. This finding suggests that PFOS did not cross the blood−brain barrier during the 48 h exposure. A previous study used MSI to detect PFOS in dissected murine tissues (liver, kidney, and brain) after gastric infusion with 1000 μg PFOS/kg/day for 2 months. The authors also did not detect PFOS in the brain.[5] The blood−brain barrier is a biochemical border of endothelial cells that are linked with tight junctions.[60] Transporters facilitate the movement of biomolecules across this boundary, and the tight junctions limit paracellular leakage.[60] Without facilitated transport, PFOS should not be able to enter the brain.[60] Yet, previous studies using brain homogenates indicated that PFOS

https://doi.org/10.1021/acs.est.5c17483
Environ. Sci. Technol. 2026, 60, 3121−3134

does accumulate in the brain of various exposed organisms.[13,61−63] Our results provide a plausible explanation for this discrepancy due to the intriguing observation of PFOS accumulation in the pineal gland. This neuroendocrine gland is located in the center of the brain in all vertebrates, including humans, and it is not protected by the blood−brain barrier.[50] Similar to our UHPLC-TIMS-PASEF-MS analysis of brain homogenate (Figure 4), the gland could have been included in brain homogenates used in the other studies, resulting in a strong PFOS signal in the homogenate. Further investigation of this possibility is warranted to truly assess the ability of PFOS to cross the blood−brain barrier.

The main function of the pineal gland is to produce and secrete the hormone melatonin in response to information about the light-dark cycle perceived within the environment. The secreted melatonin in turn regulates the circadian rhythm.[50] Apart from this well-characterized biological function, melatonin also mediates other processes.[50] These functions include developmental regulation[64] and anti-inflammatory properties, and the ability of melatonin to scavenge free radicals and reactive oxygen species as an antioxidant with high affinity.[65−67] A recent study showed that melatonin exerted a protective effect against PFOS-induced reproductive toxicity via anti-inflammatory and antioxidant pathways.[65] Melatonin also plays an important role in neuroprotection and neuronal plasticity. In fact, the maximum secretion of melatonin in humans happens during childhood and adolescence where also brain development and neuronal plasticity is at its highest.[68] Abnormal melatonin secretion has been connected to autism spectrum disorders (ASD).[68−72] Since PFOS exposure has also been associated with ASD,[73] the evidence of PFOS accumulation in the pineal gland may very well be the missing link between these observations. Based on the results presented herein, future research focusing on the connection between the effects of PFOS and melatonin homeostasis is urgently warranted.

It is important to mention that our experiment was terminated after 48 h, so redistribution past this time point was not captured. Studies suggest that over time, PFOS may be able to interfere with the tight junctions between the endothelial cells of the blood−brain barrier and allow PFOS to cross it.[62] The study duration presented here may not have been long enough to capture such an effect. Nevertheless, it is notable that PFOS bioaccumulation occurred within this relatively brief time frame at concentration ranges that were environmentally relevant.

All annotated lipids disrupted by PFOS in the olfactory epithelium and pineal gland were glycerophospholipids (GPs). As a principal component of cell membranes, GPs play an essential role in brain and systemic metabolism. In the human central nervous system, diverse GP species comprise 20−25% of adult dry brain weight and their relative ratio in membranes influence properties such as curvature, reactivity, and hydration.[74] Beyond their structural role, GPs also participate in diverse cellular functions such as signaling, membrane transport, DNA replication, apoptosis, and necrosis.[75] Phosphatidylcholines (PCs) and phosphatidylserines (PSs) have been implicated in cognitive and neurological function,[75] highlighting the importance of lipid homeostasis for brain health. Indeed, dysregulation of GP metabolism has been associated with neurodegenerative[76,77] and developmental disorders.[78]

Certain GPs appear to be particularly sensitive to disruption by PFOS. In this study, phosphatidylethanolamines (PEs) and phosphatidylglycerol (PGs) comprised the greatest number of PFOS-affected lipids, in addition to single species belonging to phosphatidylinositol (PI), phosphatidic acid (PA), and PS subclasses (Tables S7−S9). Epidemiological and experimental studies frequently report PEs and other diacyl-containing phospholipids to be associated with or modulated by PFAS, including PFOS, PFOA, PFHxS, GenX, and PFUnDA.[77,79−83] The observed effects include both upregulation and downregulation of GPs depending on the species, tissue type, and dose, but while specific effects appear context-dependent, GPs, and PEs specifically, emerge as consistent PFAS targets. Comprising 20−30% of all membrane lipids and up to 80% of inner leaflet lipids,[75] PEs play a critical role in energy metabolism,[84] so dysregulation could have consequences on membrane and metabolic function, especially in lipid-rich tissues like the brain. During neurodevelopment, such dysregulation may have an even more pronounced effect due to lipidomic shifts occurring in the developing brain. One lipid that was modulated by PFOS exposure in the pineal gland, PA (38:3), was a direct match with a lipid that increased in the mouse brain during development.[85] It is important to note that certain lipid classes ionize in the positive ion mode (e.g., phosphatidylcholines), and only the negative ion mode was employed in this study. To obtain the complete picture of GP dysregulation in responses to PFOS, additional experiments will be performed in the future, as identifying lipids that are both implicated in neurodevelopment and sensitive to PFAS disruption may help to uncover mechanisms of neurodevelopmental toxicity.

A common feature among all annotated lipids disrupted by PFOS in the olfactory epithelium and pineal gland is also their diacylglycerol (DAG) backbone. DAG is a critical signaling intermediate generated from phospholipids by lipase action[86] and serves as both a precursor to triacylglycerols (TGs) and an effector of intracellular signaling pathways.[87] Due to the involvement of DAG in many signaling processes, disruption of DAG-containing phospholipids by PFOS could have broad implications, including metabolic regulation and neurotransmission. DAG, therefore, represents a strong candidate for future investigations of elucidating toxic PFAS effects, with behavioral evaluations being an interesting avenue to explore further.

In conclusion, the present study shows how MSI greatly augments our analytical toolbox, uncovering new dimensions in our understanding of wildlife and human exposomes. This cutting-edge technology can support unbiased screening of contaminants and their distribution in wildlife biological compartments, which is essential for the characterization of their toxic effects and risks to humans and wildlife.

■ ASSOCIATED CONTENT

Data Availability Statement

The MSI data is available via the MetaSpace repository under the project "neurOmics" (https://metaspace2020.org/project/neuromics-2025). The LC-TIMS-MS data is available via the MassIVE repository under the accession number: MSV000097560.

Supporting Information

The Supporting Information is available free of charge at https://pubs.acs.org/doi/10.1021/acs.est.5c17483.

https://doi.org/10.1021/acs.est.5c17483
Environ. Sci. Technol. 2026, 60, 3121−3134

Experimental setup; quality control and performance of the MSI method; summary of the results for the four MSI slides not shown in the main text; region-specific intensities of the PFOS signal; PFOS measurement in serum; dose−response curves for features significantly affected by PFOS in brain homogenate and serum; plots of exposure-related PFAS compounds (diagnostics plot and distribution of these); additional tables show: experimental parameters, including water quality, animal weight, and exposure verification; settings of the analytical instruments; details and annotation for the significantly affected compounds resulting from MSI analysis and dose−response modeling; and supporting text to describe the analytical method for exposure verification (PDF)

AUTHOR INFORMATION

Corresponding Authors

Rikke Poulsen − *University of Victoria, Department of Biochemistry and Microbiology, Victoria, British Columbia V8P 5C2, Canada; University of Victoria Genome British Columbia Proteomics Centre, Victoria, British Columbia V8Z 7 × 8, Canada; Aarhus University, Department of Environmental Science, 4000 Roskilde, Denmark*; Email: rikkepoulsen@envs.au.dk

Helena Pětrošová − *University of Victoria, Department of Biochemistry and Microbiology, Victoria, British Columbia V8P 5C2, Canada; University of Victoria Genome British Columbia Proteomics Centre, Victoria, British Columbia V8Z 7 × 8, Canada;* orcid.org/0009-0008-9756-7236; Email: hpetros@uvic.ca

Authors

Emma M. Field − *University of Victoria, Department of Biochemistry and Microbiology, Victoria, British Columbia V8P 5C2, Canada*

Angela M. Jackson − *University of Victoria Genome British Columbia Proteomics Centre, Victoria, British Columbia V8Z 7 × 8, Canada*

Haley Kuecks-Winger − *University of Victoria, Department of Biochemistry and Microbiology, Victoria, British Columbia V8P 5C2, Canada*

Anita A. Thambirajah − *University of Victoria, Department of Biochemistry and Microbiology, Victoria, British Columbia V8P 5C2, Canada*

David R. Goodlett − *University of Victoria Genome British Columbia Proteomics Centre, Victoria, British Columbia V8Z 7 × 8, Canada*

Caren C. Helbing − *University of Victoria, Department of Biochemistry and Microbiology, Victoria, British Columbia V8P 5C2, Canada;* orcid.org/0000-0002-8861-1070

Complete contact information is available at: https://pubs.acs.org/10.1021/acs.est.5c17483

Author Contributions

R.P.: conceptualization, formal analysis, funding acquisition, investigation, methodology, and writing—original draft preparation. E.M.F.: investigation, methodology, data curation, and writing—original draft preparation. A.M.J.: conceptualization, investigation, methodology, and writing—review and editing. H.K.-W.: investigation, methodology, and writing—review and editing. A.T.: conceptualization, investigation, and writing—review and editing. D.R.G.: funding acquisition, project administration, resources, and writing—review and editing. C.C.H.: conceptualization, funding acquisition, methodology, project administration, resources, supervision, and writing—review and editing. H.P.: conceptualization, funding acquisition, methodology, project administration, supervision, and writing—review and editing.

Notes

The authors declare no competing financial interest.

ACKNOWLEDGMENTS

The authors thank Christian Romanowski and Dr. Vanessa Thompson for help with the sample collection, Derek Smith for help with the LC-TIMS-ToF method, and Dr. Rossana Bossi and Birgit Groth for help with the PFOS exposure verification. R.P. acknowledges financial support from the European Union's HORIZON TMA MSCA Postdoctoral Fellowships − Global Fellowships under grant agreement No. 101068090. C.C.H. acknowledges funding from the Natural Science and Engineering Research Council of Canada (NSERC) Discovery grant (RGPIN-2018-03816). E.M.F. is a recipient of an NSERC CGS-M scholarship. D.R.G., H.P., and the work at the University of Victoria Genome BC Proteomics Centre (UVic-PC) were supported by funding to The Metabolomics Innovation Centre (TMIC) from Canadian Foundation for Innovation Major Sciences Initiative (42495), Genome British Columbia (365MET and 375MET), and Genome Canada (MC5). The UVic-PC is also grateful to Pacifican for infrastructure funding used to purchase the timsTOF flex MALDI-2 mass spectrometer (000022591).

REFERENCES

(1) Duncan, K. D.; Pětrošová, H.; Lum, J. J.; Goodlett, D. R. Mass Spectrometry Imaging Methods for Visualizing Tumor Heterogeneity. *Curr. Opin. Biotechnol.* **2024**, *86*, No. 103068.

(2) Herruzo-Ruiz, A. M.; Peralbo-Molina, Á.; López, C.-M.; Michán, C.; Alhama, J.; Chicano-Gálvez, E. Mass Spectrometry Imaging in Environmental Monitoring: From a Scarce Existing Past to a Promising Future. *Trends Environ. Anal. Chem.* **2024**, *42*, No. e00228.

(3) Yang, C.; Lee, H. K.; Zhang, Y.; Jiang, L. L.; Chen, Z. F.; Chung, A. C. K.; Cai, Z. In Situ Detection and Imaging of PFOS in Mouse Kidney by Matrix-Assisted Laser Desorption/Ionization Imaging Mass Spectrometry. *Anal. Chem.* **2019**, *91* (14), 8783−8788.

(4) Shi, R.; Chen, Y.; Wu, W.; Diao, X.; Chen, L.; Liu, X.; Wu, H.; Wang, J.; Zhu, L.; Cai, Z. Mass Spectrometry-Based Spatial Multiomics Revealed Bioaccumulation Preference and Region-Specific Responses of PFOS in Mice Cardiac Tissue. *Environ. Sci. Technol.* **2025**, *59*, 1957−1968.

(5) Li, X.; Li, T.; Wang, Z.; Wei, J.; Liu, J.; Zhang, Y.; Zhao, Z. Distribution of Perfluorooctane Sulfonate in Mice and Its Effect on Liver Lipidomic. *Talanta* **2021**, *226*, No. 122150.

(6) Chen, Y.; Jiang, L.; Zhang, R.; Shi, Z.; Xie, C.; Hong, Y.; Wang, J.; Cai, Z. Spatially Revealed Perfluorooctane Sulfonate-Induced Nephrotoxicity in Mouse Kidney Using Atmospheric Pressure MALDI Mass Spectrometry Imaging. *Sci. Total Environ.* **2022**, *838*, No. 156380.

(7) Ho, T. C.; Wan, H. T.; Lee, W. K.; Lam, T. K. Y.; Lin, X.; Chan, T. F.; Lai, K. P.; Wong, C. K. C. Effects of In Utero PFOS Exposure on Epigenetics and Metabolism in Mouse Fetal Livers. *Environ. Sci. Technol.* **2023**, *57* (40), 14892−14903.

(8) Domingo, J. L. A Review of the Occurrence and Distribution of Per- and Polyfluoroalkyl Substances (PFAS) in Human Organs and Fetal Tissues. *Environ. Res.* **2025**, *272*, No. 121181.

(9) Fenton, S. E.; Ducatman, A.; Boobis, A.; DeWitt, J. C.; Lau, C.; Ng, C.; Smith, J. S.; Roberts, S. M. Per- and Polyfluoroalkyl Substance

Toxicity and Human Health Review: Current State of Knowledge and Strategies for Informing Future Research. *Environ. Toxicol. Chem.* **2020**, *40* (3), 606−630.
(10) Roy, V. C.; Bala, R.; Mehta, S. Poly- and per-Fluoroalkyl Substances Toxicity on Skeletal and Cognitive Well-Being: A Comprehensive Review. *J. Environ. Sci. Health, Part C* **2025**, *43*, 159−183.
(11) Gewurtz, S. B.; Bhavsar, S. P.; Petro, S.; Mahon, C. G.; Zhao, X.; Morse, D.; Reiner, E. J.; Tittlemier, S. A.; Braekevelt, E.; Drouillard, K. High Levels of Perfluoroalkyl Acids in Sport Fish Species Downstream of a Firefighting Training Facility at Hamilton International Airport, Ontario, Canada. *Environ. Int.* **2014**, *67*, 1−11.
(12) Davidsen, N.; Ramhøj, L.; Lykkebo, C. A.; Kugathas, I.; Poulsen, R.; Rosenmai, A. K.; Evrard, B.; Darde, T. A.; Axelstad, M.; Bahl, M. I.; Hansen, M.; Chalmel, F.; Licht, T. R.; Svingen, T. PFOS-Induced Thyroid Hormone System Disrupted Rats Display Organ-Specific Changes in Their Transcriptomes. *Environ. Pollut.* **2022**, *305* (April), No. 119340.
(13) Bharal, B.; Ruchitha, C.; Kumar, P.; Pandey, R.; Rachamalla, M.; Niyogi, S.; Naidu, R.; Kaundal, R. K. Neurotoxicity of Per- and Polyfluoroalkyl Substances: Evidence and Future Directions. *Sci. Total Environ.* **2024**, *955*, No. 176941.
(14) European Chemicals Agency. Per- and polyfluoroalkyl substances (PFAS)https://echa.europa.eu/hot-topics/perfluoroalkyl-chemicals-pfas. https://echa.europa.eu/hot-topics/perfluoroalkyl-chemicals-pfas (accessed May 03, 2025).
(15) Health Canada. Perfluorooctane sulfonate (PFOS). https://www.canada.ca/en/health-canada/services/chemical-substances/other-chemical-substances-interest/perfluorooctane-sulfonate.htmlhttps://www.canada.ca/en/health-canada/services/chemical-substances/other-chemical-substances-interest/perfluorooctane-sulfonate.html (accessed May 03, 2025).
(16) Jarvis, A. L.; Justice, J. R.; Elias, M. C.; Schnitker, B.; Gallagher, K. Perfluorooctane Sulfonate in US Ambient Surface Waters: A Review of Occurrence in Aquatic Environments and Comparison to Global Concentrations. *Environ. Toxicol. Chem.* **2021**, *40* (9), 2425−2442.
(17) Awad, E.; Zhang, X.; Bhavsar, S. P.; Petro, S.; Crozier, P. W.; Reiner, E. J.; Fletcher, R.; Tittlemier, S. A.; Braekevelt, E. Long-Term Environmental Fate of Perfluorinated Compounds after Accidental Release at Toronto Airport. *Environ. Sci. Technol.* **2011**, *45* (19), 8081−8089.
(18) Koch, A.; Kärrman, A.; Yeung, L. W. Y.; Jonsson, M.; Ahrens, L.; Wang, T. Point Source Characterization of Per- and Polyfluoroalkyl Substances (PFASs) and Extractable Organofluorine (EOF) in Freshwater and Aquatic Invertebrates. *Environ. Sci. Process Impacts* **2019**, *21* (11), 1887−1898.
(19) Bhavsar, S. P.; Fowler, C.; Day, S.; Petro, S.; Gandhi, N.; Gewurtz, S. B.; Hao, C.; Zhao, X.; Drouillard, K. G.; Morse, D. High Levels, Partitioning and Fish Consumption Based Water Guidelines of Perfluoroalkyl Acids Downstream of a Former Firefighting Training Facility in Canada. *Environ. Int.* **2016**, *94*, 415−423.
(20) Longpré, D.; Lorusso, L.; Levicki, C.; Carrier, R.; Cureton, P. PFOS, PFOA, LC-PFCAS, and Certain Other PFAS: A Focus on Canadian Guidelines and Guidance for Contaminated Sites Management. *Environ. Technol. Innovation* **2020**, *18*, No. 100752.
(21) Dewitt, J. C. *Toxicological Effects of Perfluoroalkyl and Polyfluoroalkyl Substances*; DeWitt, J. C., Ed.; Springer International Publishing, 2015 DOI: 10.1007/978-3-319-15518-0.
(22) Beale, D. J.; Nilsson, S.; Bose, U.; Bourne, N.; Stockwell, S.; Broadbent, J. A.; Gonzalez-Astudillo, V.; Braun, C.; Baddiley, B.; Limpus, D.; Walsh, T.; Vardy, S. Bioaccumulation and Impact of Maternal PFAS Offloading on Egg Biochemistry from Wild-Caught Freshwater Turtles (Emydura Macquarii Macquarii). *Sci. Total Environ.* **2022**, *817*, No. 153019.
(23) Grunfeld, D. A.; Gilbert, D.; Hou, J.; Jones, A. M.; Lee, M. J.; Kibbey, T. C. G.; O'Carroll, D. M. Underestimated Burden of Per- and Polyfluoroalkyl Substances in Global Surface Waters and Groundwaters. *Nat. Geosci.* **2024**, *17* (4), 340−346.
(24) Gobelius, L.; Hedlund, J.; Dürig, W.; Tröger, R.; Lilja, K.; Wiberg, K.; Ahrens, L. Per- and Polyfluoroalkyl Substances in Swedish Groundwater and Surface Water: Implications for Environmental Quality Standards and Drinking Water Guidelines. *Environ. Sci. Technol.* **2018**, *52* (7), 4340−4349.
(25) Dauchy, X.; Boiteux, V.; Colin, A.; Bach, C.; Rosin, C.; Munoz, J.-F. Poly- and Perfluoroalkyl Substances in Runoff Water and Wastewater Sampled at a Firefighter Training Area. *Arch. Environ. Contam. Toxicol.* **2019**, *76* (2), 206−215.
(26) Burlibaşa, L.; Gavrilă, L. Amphibians as Model Organisms for Study Environmental Genotoxicity. *Appl. Ecol. Environ. Res.* **2011**, *9* (1), 1−15.
(27) Thambirajah, A. A.; Koide, E. M.; Imbery, J. J.; Helbing, C. C. Contaminant and Environmental Influences on Thyroid Hormone Action in Amphibian Metamorphosis. *Front. Endocrinol.* **2019**, *10*, No. 276.
(28) Hayes, T. B.; Hansen, M. From Silent Spring to Silent Night: Agrochemicals and the Anthropocene. *Elem.: Sci. Anthropocene* **2017**, *5*, No. 57.
(29) Paul, B.; Sterner, Z. R.; Buchholz, D. R.; Shi, Y.-B.; Sachs, L. M. Thyroid and Corticosteroid Signaling in Amphibian Metamorphosis. *Cells* **2022**, *11* (10), No. 1595.
(30) Hayes, T. B. Amphibian Metamorphosis: An Integrative Approach. *Am. Zool.* **1997**, *37* (2), 121−123.
(31) Weber, R. *Anuran Metamorphosis*; Academic Press, Inc., 1996, DOI: 10.1016/B978-0-12-283245-1.50018.
(32) Buchholz, D. R. More Similar than You Think: Frog Metamorphosis as a Model of Human Perinatal Endocrinology. *Dev. Biol.* **2015**, *408* (2), 188−195.
(33) Xiao, Y.; Deng, J.; Fang, L.; Tu, L.; Luan, T. Mapping the Distribution of Perfluoroalkyl Substances in Zebrafishes by Liquid Extraction Surface Analysis Mass Spectrometry. *Talanta* **2021**, *231*, No. 122377.
(34) Donslund, M. F. S.; Granborg, J. R.; Niklas, A. A.; Janfelt, C.; Sloth, J. J.; Philipsen, P. A.; Wulf, H. C.; Lerche, C. M. Evaluation of the Photocarcinogenic Potential of Perfluorooctanoic Acid in Mice after Topical and Oral Exposure. *J. Invest. Dermatol.* **2025**, *145* (6), 1509−1512.e6.
(35) Bian, Y.; He, M. Y.; Ling, Y.; Wang, X. J.; Zhang, F.; Feng, X. S.; Zhang, Y.; Xing, S. G.; Li, J.; Qiu, X.; Li, Y. R. Tissue Distribution Study of Perfluorooctanoic Acid in Exposed Zebrafish Using MALDI Mass Spectrometry Imaging. *Environ. Pollut.* **2022**, *293*, No. 118505.
(36) Teymoorian, T.; Delon, L.; Munoz, G.; Sauvé, S. Target and Suspect Screening Reveal PFAS Exceeding European Union Guideline in Various Water Sources South of Lyon, France. *Environ. Sci. Technol. Lett.* **2025**, *12* (3), 327−333.
(37) Maher, S. K.; Wojnarowicz, P.; Ichu, T.-A.; Veldhoen, N.; Lu, L.; Lesperance, M.; Propper, C. R.; Helbing, C. C. Rethinking the Biological Relationships of the Thyroid Hormones, l-Thyroxine and 3,5,3′-Triiodothyronine. *Comp. Biochem. Physiol., Part D: Genomics Proteomics* **2016**, *18*, 44−53.
(38) Helbing, C.; Gergely, G.; Atkinson, B. G. Sequential Up-regulation of Thyroid Hormone β Receptor, Ornithine Transcarbamylase, and Carbamyl Phosphate Synthetase MRNAs in the Liver of Rana Catesbeiana Tadpoles during Spontaneous and Thyroid Hormone-induced Metamorphosis. *Dev. Genet.* **1992**, *13* (4), 289−301.
(39) R Core Team. *R: A Language and Environment for Statistical Computing* R Foundation for Statistical Computing: Vienna; 2020. https://www.r-project.org/.
(40) Bemis, K. A.; Föll, M. C.; Guo, D.; Lakkimsetty, S. S.; Vitek, O. Cardinal v.3: A Versatile Open-Source Software for Mass Spectrometry Imaging Analysis. *Nat. Methods* **2023**, *20* (12), 1883−1886.
(41) Posit team. *RStudio: Integrated Development Environment for R.. Posit Software*; PBC: Boston, MA, 2024.
(42) Bates, D.; Mächler, M.; Bolker, B.; Walker, S. Fitting Linear Mixed-Effects Models Using Lme4. *J. Stat Softw* **2015**, *67* (1), 1−48.
(43) Hothorn, T.; Bretz, F.; Westfall, P. Simultaneous Inference in General Parametric Models. *Biom. J.* **2008**, *50* (3), 346−363.

https://doi.org/10.1021/acs.est.5c17483
Environ. Sci. Technol. 2026, 60, 3121−3134

(44) Kolde, R. Pheatmap: Pretty Heatmaps. R Package Version 1.0.12.. 2019, pp 1−8.
(45) Viant, M. R.; Ebbels, T. M. D.; Beger, R. D.; Ekman, D. R.; Epps, D. J. T.; Kamp, H.; Leonards, P. E. G.; Loizou, G. D.; MacRae, J. I.; van Ravenzwaay, B.; Rocca-Serra, P.; Salek, R. M.; Walk, T.; Weber, R. J. M. Use Cases, Best Practice and Reporting Standards for Metabolomics in Regulatory Toxicology. *Nat. Commun.* **2019**, *10* (1), No. 3041.
(46) Post, J. M.; Lerner, R.; Schwitter, C.; Lutz, B.; Lomazzo, E.; Bindila, L. Lipidomics and Transcriptomics in Neurological Diseases *J. Visualized Exp.* 2022; Vol. *2022* 181 DOI: 10.3791/59423.
(47) Liebisch, G.; Fahy, E.; Aoki, J.; Dennis, E. A.; Durand, T.; Ejsing, C. S.; Fedorova, M.; Feussner, I.; Griffiths, W. J.; Köfeler, H.; Merrill, A. H.; Murphy, R. C.; O'Donnell, V. B.; Oskolkova, O.; Subramaniam, S.; Wakelam, M. J. O.; Spener, F. Update on LIPID MAPS Classification, Nomenclature, and Shorthand Notation for MS-Derived Lipid Structures. *J. Lipid Res.* **2020**, *61* (12), 1539−1555.
(48) Delignette-Muller, M. L.; Siberchicot, A.; Larras, F.; Billoir, E. DRomics, a Workflow to Exploit Dose-Response Omics Data in Ecotoxicology. *Peer Commu. J.* **2023**, *3*, No. e90.
(49) Larras, F.; Billoir, E.; Baillard, V.; Siberchicot, A.; Scholz, S.; Wubet, T.; Tarkka, M.; Schmitt-Jansen, M.; Delignette-Muller, M. L. DRomics: A Turnkey Tool to Support the Use of the Dose-Response Framework for Omics Data in Ecological Risk Assessment. *Environ. Sci. Technol.* **2018**, *52* (24), 14461−14468.
(50) Arendt, J.; Aulinas, A. *Physiology of the Pineal Gland and Melatonin*; Feingold, K. R.; Anawalt, B.; Blackman, M. R., Eds.; MDText.com, Inc.: South Dartmouth (MA), 2000.
(51) Villeneuve, D. L.; Crump, D.; Hecker, M.; Hutchinson, T. H.; Lalone, C. A.; Landesmann, B.; Lettieri, T.; Munn, S.; Nepelska, M.; Ann, M.; Vergauwen, L.; Whelan, M. Adverse Outcome Pathway (AOP) Development I: Strategies and Principles. *Toxicol. Sci.* **2014**, *142* (2), 312−320.
(52) Goodwin, R. J. A.; Nilsson, A.; Borg, D.; Langridge-Smith, P. R. R.; Harrison, D. J.; Mackay, C. L.; Iverson, S. L.; Andrén, P. E. Conductive Carbon Tape Used for Support and Mounting of Both Whole Animal and Fragile Heat-Treated Tissue Sections for MALDI MS Imaging and Quantitation. *J. Proteomics* **2012**, *75* (16), 4912−4920.
(53) Vandenbosch, M.; Nauta, S. P.; Svirkova, A.; Poeze, M.; Heeren, R. M. A.; Siegel, T. P.; Cuypers, E.; Marchetti-Deschmann, M. Sample Preparation of Bone Tissue for MALDI-MSI for Forensic and (Pre)Clinical Applications. *Anal. Bioanal. Chem.* **2021**, *413* (10), 2683−2694.
(54) Saigusa, D.; Saito, R.; Kawamoto, K.; Uruno, A.; Kano, K.; Aoki, J.; Yamamoto, M.; Kawamoto, T. Conductive Adhesive Film Expands the Utility of Matrix-Assisted Laser Desorption/Ionization Mass Spectrometry Imaging. *Anal. Chem.* **2019**, *91* (14), 8979−8986.
(55) Reynolds, A. J.; Smith, A. M.; Qiu, T. A. Detection, Quantification, and Isomer Differentiation of Per- and Polyfluoroalkyl Substances (PFAS) Using MALDI-TOF with Trapped Ion Mobility. *J. Am. Soc. Mass Spectrom.* **2024**, *35* (2), 317−325.
(56) Yang, C.; Lee, H. K.; Zhang, Y.; Jiang, L. L.; Chen, Z. F.; Chung, A. C. K.; Cai, Z. In Situ Detection and Imaging of PFOS in Mouse Kidney by Matrix-Assisted Laser Desorption/Ionization Imaging Mass Spectrometry. *Anal. Chem.* **2019**, *91* (14), 8783−8788.
(57) Hepper, P. G.; Waldman, B. Embryonic Olfactory Learning in Frogs. *Q. J. Exp. Psychol., Sect. B* **1992**, *44* (3−4b), 179−197.
(58) Field, E. M.; Corrie, L. M.; Kuecks-Winger, H. N.; Helbing, C. C. Utilization of Temperature-Mediated Activation of Thyroid Hormone-Induced Molecular Memory to Evaluate Early Signaling Events in the Olfactory Epithelium of Rana [Lithobates] Catesbeiana Tadpoles. *Comp. Biochem. Physiol., Part D: Genomics Proteomics* **2024**, *49*, No. 101189.
(59) Heerema, J. L.; Bogart, S. J.; Helbing, C. C.; Pyle, G. G. Olfactory Epithelium Ontogenesis and Function in Postembryonic North American Bullfrog (Rana (Lithobates) Catesbeiana) Tadpoles. *Can. J. Zool.* **2020**, *98* (6), 367−375.
(60) Abbott, N. J.; Patabendige, A. A. K.; Dolman, D. E. M.; Yusof, S. R.; Begley, D. J. Structure and Function of the Blood−Brain Barrier. *Neurobiol. Dis.* **2010**, *37* (1), 13−25.
(61) Cao, Y.; Ng, C. Absorption, Distribution, and Toxicity of per- and Polyfluoroalkyl Substances (PFAS) in the Brain: A Review. *Environ. Sci. Process Impacts* **2021**, *23* (11), 1623−1640.
(62) Yu, Y.; Wang, C.; Zhang, X.; Zhu, J.; Wang, L.; Ji, M.; Zhang, Z.; Ji, X.-M.; Wang, S.-L. Perfluorooctane Sulfonate Disrupts the Blood Brain Barrier through the Crosstalk between Endothelial Cells and Astrocytes in Mice. *Environ. Pollut.* **2020**, *256*, No. 113429.
(63) Pedersen, K. E.; Basu, N.; Letcher, R.; Greaves, A. K.; Sonne, C.; Dietz, R.; Styrishave, B. Brain Region-Specific Perfluoroalkylated Sulfonate (PFSA) and Carboxylic Acid (PFCA) Accumulation and Neurochemical Biomarker Responses in East Greenland Polar Bears (Ursus Maritimus). *Environ. Res.* **2015**, *138*, 22−31.
(64) Bae, S.-E.; Wright, I. K.; Wyse, C.; Samson-Desvignes, N.; Le Blanc, P.; Laroche, S.; Hazlerigg, D. G.; Johnston, J. D. Regulation of Pituitary MT1Melatonin Receptor Expression by Gonadotrophin-Releasing Hormone (GnRH) and Early Growth Response Factor-1 (Egr-1): In Vivo and In Vitro Studies. *PLoS One* **2014**, *9* (3), No. e90056.
(65) Han, J.; Lu, Z.; Qi, Y.; Liu, T.; Li, Y.; Han, H.; Zhao, C.; Ma, X. Melatonin Attenuates PFOS-Induced Reproductive Toxicity of Pregnant Mice Due to Placental Damage Via Antioxidant, Anti-Aging and Anti-Inflammatory Pathways. *Birth Defects Res.* **2024**, *116* (12), No. e2423.
(66) Yang, L.; Cheng, J.; Xu, D.; Zhang, Z.; Hua, R.; Chen, H.; Duan, J.; Li, X.; Li, Q. Melatonin Ameliorates Diquat-Induced Testicular Toxicity via Reducing Oxidative Stress, Inhibiting Apoptosis, and Maintaining the Integrity of Blood-Testis Barrier in Mice. *Toxics* **2023**, *11* (2), No. 160.
(67) Maitra, S. K.; Hasan, K. N. The Role of Melatonin as a Hormone and an Antioxidant in the Control of Fish Reproduction. *Front. Endocrinol.* **2016**, *7*, No. 38.
(68) Biggio, G.; Biggio, F.; Talani, G.; Mostallino, M. C.; Aguglia, A.; Aguglia, E.; Palagini, L. Melatonin: From Neurobiology to Treatment. *Brain Sci.* **2021**, *11*, No. 1121.
(69) Jin, Y.; Choi, J.; Won, J.; Hong, Y. The Relationship between Autism Spectrum Disorder and Melatonin during Fetal Development. *Molecules* **2018**, *23*, No. 198.
(70) Kulman, G.; Lissoni, P.; Rovelli, F.; Roselli, M. G.; Brivio, F.; Sequeri, P. Evidence of Pineal Endocrine Hypofunction in Autistic Children. *Neuroendocrinol. Let.* **2000**, *21* (1), 31−34.
(71) Pagan, C.; Delorme, R.; Callebert, J.; Goubran-Botros, H.; Amsellem, F.; Drouot, X.; Boudebesse, C.; Dudal, K. L.; Ngo-Nguyen, N.; Laouamri, H.; Gillberg, C.; Leboyer, M.; Bourgeron, T.; Launay, J. M. The Serotonin-N-Acetylserotonin-Melatonin Pathway as a Biomarker for Autism Spectrum Disorders. *Transl. Psychiatry* **2014**, *4* (11), No. e479.
(72) Coogan, A. N.; McGowan, N. M. A Systematic Review of Circadian Function, Chronotype and Chronotherapy in Attention Deficit Hyperactivity Disorder. *ADHD Atten. Deficit Hyperactivity Disord.* **2017**, 129−147.
(73) Currie, S. D.; Wang, J.-S.; Tang, L. Impacts of PFAS Exposure on Neurodevelopment: A Comprehensive Literature Review. *Environments* **2024**, *11* (9), No. 188.
(74) Farooqui, A. A.; Horrocks, L. A.; Farooqui, T. Glycerophospholipids in Brain: Their Metabolism, Incorporation into Membranes, Functions, and Involvement in Neurological Disorders. *Chem. Phys. Lipids* **2000**, *106* (1), 1−29.
(75) Castro-Gómez, P.; Garcia-Serrano, A.; Visioli, F.; Fontecha, J. Relevance of Dietary Glycerophospholipids and Sphingolipids to Human Health. *Prostaglandins, Leukotrienes Essent. Fatty Acids* **2015**, *101*, 41−51.
(76) Burg, T.; Van Den Bosch, L. Glycerophospholipids in ALS: Insights into Disease Mechanisms and Clinical Implication. *Mol. Neurodegener.* **2025**, *20* (1), No. 85.
(77) Yao, W.; Xu, J.; Tang, W.; Gao, C.; Tao, L.; Yu, J.; Lv, J.; Wang, H.; Fan, Y.; Xu, D. X.; Huang, Y. Developmental Toxicity of

Perfluorohexane Sulfonate at Human Relevant Dose during Pregnancy via Disruption in Placental Lipid Homeostasis. *Environ. Int.* **2023**, *177*, No. 108014.
(78) Lamari, F.; Rossignol, F.; Mitchell, G. A. Glycerophospholipids: Roles in Cell Trafficking and Associated Inborn Errors. *J. Inherited Metab. Dis.* **2025**, *48*, No. e70019.
(79) India-Aldana, S.; Yao, M.; Midya, V.; Colicino, E.; Chatzi, L.; Chu, J.; Gennings, C.; Jones, D. P.; Loos, R. J. F.; Setiawan, V. W.; Smith, M. R.; Walker, R. W.; Barupal, D.; Walker, D. I.; Valvi, D. PFAS Exposures and the Human Metabolome: A Systematic Review of Epidemiological Studies. *Curr. Pollut. Rep.* **2023**, *9*, 510−568, DOI: 10.1007/s40726-023-00269-4.
(80) Stoffels, C. B. A.; Angerer, T. B.; Robert, H.; Poupin, N.; Lakhal, L.; Frache, G.; Mercier-Bonin, M.; Audinot, J. N. Lipidomic Profiling of PFOA-Exposed Mouse Liver by Multi-Modal Mass Spectrometry Analysis. *Anal. Chem.* **2023**, *95* (16), 6568−6576.
(81) Yang, Z.; Fu, L.; Cao, M.; Li, F.; Li, J.; Chen, Z.; Guo, A.; Zhong, H.; Li, W.; Liang, Y.; Luo, Q. PFAS-Induced Lipidomic Dysregulations and Their Associations with Developmental Toxicity in Zebrafish Embryos. *Sci. Total Environ.* **2023**, *861*, No. 160691.
(82) Kirkwood-Donelson, K. I.; Chappel, J.; Tobin, E.; Dodds, J. N.; Reif, D. M.; DeWitt, J. C.; Baker, E. S. Investigating Mouse Hepatic Lipidome Dysregulation Following Exposure to Emerging Per- and Polyfluoroalkyl Substances (PFAS). *Chemosphere* **2024**, *354*, No. 141654.
(83) Hyötyläinen, T.; Bodin, J.; Duberg, D.; Dirven, H.; Nygaard, U. C.; Orešič, M. Lipidomic Analyses Reveal Modulation of Lipid Metabolism by the PFAS Perfluoroundecanoic Acid (PFUnDA) in Non-Obese Diabetic Mice. *Front. Genet.* **2021**, *12*, No. 721507.
(84) van der Veen, J. N.; Kennelly, J. P.; Wan, S.; Vance, J. E.; Vance, D. E.; Jacobs, R. L. The Critical Role of Phosphatidylcholine and Phosphatidylethanolamine Metabolism in Health and Disease. *Biochim. Biophys. Acta, Biomembr.* **2017**, *1859*, 1558−1572.
(85) Oliveira, M.; Koshibu, K.; Rytz, A.; Giuffrida, F.; Sultan, S.; Patin, A.; Gaudin, M.; Tomezyk, A.; Steiner, P.; Schneider, N. Early Life to Adult Brain Lipidome Dynamic: A Temporospatial Study Investigating Dietary Polar Lipid Supplementation Efficacy. *Front. Nutr.* **2022**, *9*, No. 898655, DOI: 10.3389/fnut.2022.898655.
(86) Eichmann, T. O.; Lass, A. DAG Tales: The Multiple Faces of Diacylglycerol - Stereochemistry, Metabolism, and Signaling. *Cell. Mol. Life Sci.* **2015**, *72* (20), 3931−3952.
(87) Lee, D.; Kim, E.; Tanaka-Yamamoto, K. Diacylglycerol Kinases in the Coordination of Synaptic Plasticity. *Front. Cell Dev. Biol.* **2016**, *4*, No. 92.

https://doi.org/10.1021/acs.est.5c17483
Environ. Sci. Technol. 2026, 60, 3121−3134